

## Research



**Cite this article:** Fijan D, Wilson M. 2023 Thermodynamic anomalies, polyamorphism and all that. *Phil. Trans. R. Soc. A* **381**: 20220336. <https://doi.org/10.1098/rsta.2022.0336>

Received: 12 February 2023

Accepted: 18 May 2023

One contribution of 13 to a theme issue 'Exploring the length scales, timescales and chemistry of challenging materials (Part 1)'.

**Subject Areas:**

computational chemistry, physical chemistry

**Keywords:**

thermodynamics, phase diagrams, polymorphism

**Author for correspondence:**

Mark Wilson

e-mail: [mark.wilson@chem.ox.ac.uk](mailto:mark.wilson@chem.ox.ac.uk)

<sup>†</sup>Present address: Department of Chemical Engineering, Biointerfaces Institute, University of Michigan, Ann Arbor, MI, USA.

Thermodynamic anomalies,  
polyamorphism and all that

Domagoj Fijan<sup>†</sup> and Mark Wilson

Department of Chemistry, Physical and Theoretical Chemistry Laboratory, University of Oxford, Oxford, UK

DF, 0000-0002-4256-2074; MW, 0000-0003-4599-7943

The appearance and evolution of thermodynamics anomalies, and related properties, are studied for two classes of system, modelling those dominated by covalent and ionic interactions, respectively. Such anomalies are most familiar in the density but are also present in other thermodynamics variables such as the compressibility and heat capacity. By systematically varying key model parameters the emergence and evolution of these anomalies can be tracked across the phase space. The interaction of the anomalies can often be rationalized by thermodynamics 'rules'. The emergence of these anomalies may also be correlated with the appearance of polyamorphism, the existence of multiple amorphous states which differ in density and entropy.

This article is part of the theme issue 'Exploring the length scales, timescales and chemistry of challenging materials (Part 1)'.

## 1. Introduction

Water shows perhaps the most widely known thermodynamic anomaly, displaying a maximum in the density at  $T \sim 4^\circ\text{C}$  (at ambient pressure). However, such anomalous behaviour is not limited to water. For example, anomalous behaviour is observed in systems ranging from silicon [1,2], germanium [3] and carbon, to  $\text{BeF}_2$ ,  $\text{SiO}_2$  and  $\text{GeO}_2$  [1,4]. The detailed origin of such behaviour is subtle and often 'buried' in the balance of the dominant interatomic interactions. Si and Ge, for example, are classic 'covalent' materials,

while  $\text{BeF}_2$  and  $\text{SiO}_2$  can be considered as dominated by ionic (electrostatic) interactions. Water effectively shows a mixture of covalent and ionic interactions, as well as significant hydrogen-bonding effects [4].

Computer simulation models offer potentially unique insight into anomalous behaviour as, not only are the location of all atoms known exactly, but the precise details of the interatomic interactions can be systematically controlled and varied. Many different potential models have been applied with both electrostatic potentials (either polarizable or non-polarizable [5–13]) and covalent models, such as the Stillinger–Weber (SW) potential, originally used to model silicon, [14] displaying anomalous behaviour in the liquid and/or supercooled region of the phase diagram. Furthermore, although anomalous behaviour is most well-known for the density, related behaviour is observed in properties such as the compressibility and heat capacity [7,12,15–48]. The manner in which these anomalies interact in the phase space is governed by the laws of thermodynamics. Significant previous work has focused on how the various anomalies (and the related stability limits (SL)) interact with each other [18,36,37,49–56]. In recent work, we have derived a more complete set of interaction rules [57].

The density maximum in  $\text{H}_2\text{O}$  at  $T \sim 4^\circ\text{C}$  is specific to ambient pressure. Determining the temperature at which the anomaly appears as a function of pressure allows a locus of the turning points to be constructed which is termed a temperature of maximum density (TMD) line. In the systems listed above these appear to arise from the subtle disruption of a basically tetrahedral network as a function of temperature and/or pressure.

In general, two basic modelling strategies have traditionally been employed. Firstly, relatively accurate models are used to model specific systems, for example,  $\text{SiO}_2$  [58–61],  $\text{BeF}_2$  [9,10,61],  $\text{GeO}_2$  [61] and  $\text{H}_2\text{O}$  [15,17,18,52,61–64]. Secondly, more generic models are used, with examples including the SW [65,66], ramp [60,67–69] or core-softened [70] potentials. Recent work has highlighted how the location of critical points, focusing on both colloidal systems [71] and modified water potentials [72], depends on the detail of the underlying potential model.

Systems such as  $\text{SiO}_2$  and  $\text{BeF}_2$  are dominated by electrostatic interactions [73–76]. As a result, anions surround cations with the nearest-neighbour coordination number (the short-range order). This coordination is effectively controlled by the relative ion sizes (usually in terms of ‘radius-ratio rules’).  $\text{SiO}_2$ ,  $\text{GeO}_2$  and  $\text{BeF}_2$  show structural similarities in the sense that the nearest-neighbour coordination polyhedra are  $\text{MX}_4$  tetrahedra. However, their ordering beyond the short-range may differ as the bridging bond angles between neighbouring tetrahedra vary from  $\bar{\theta}_{\text{MXM}} \simeq 130^\circ$  for  $\text{GeO}_2$ , to  $\bar{\theta}_{\text{MXM}} \simeq 145^\circ$  for  $\text{SiO}_2$ , to  $\bar{\theta}_{\text{MXM}} \simeq 155^\circ$  for  $\text{BeF}_2$  [77]. The M–X–M bond angles are controlled by many-body (ion polarization) interactions [78,79]. Dipoles induced on the bridging anions act to introduce negative charge between neighbouring cation centres, effectively screening the cation–cation repulsive electrostatic interaction [80]. The magnitude of these dipoles depends on the magnitude of the local electric field and the anion dipole polarizability [78,79,81] and effectively controls the system topology. As a result, in an ionic model these bond angles can be controlled by a single model parameter, the (anion) dipole polarizability,  $\alpha$ . This means that generic models can be applied in which  $\alpha$  is systematically varied [81,82]. For the  $\text{MX}_2$  stoichiometry polarizable-ion models (PIMs) have been developed for  $\text{GeSe}_2$  [60],  $\text{GeO}_2$  [83],  $\text{ZnCl}_2$  [60,84] and  $\text{SiO}_2$  [85].

Systems such as silicon and water show highly complex crystalline phase diagrams which show complex changes in coordination environment on different length scales. In the disordered state silicon shows low- and high-density amorphous forms (LDA and HDA) which are characterized by showing different densities and entropies, and which display a change in (electronic) conductivity [86]. More recent experiments and simulations highlight how silicon may be more ‘water-like’, displaying additional amorphous forms [87,88].

In this paper, two classes of model will be applied to consider systems dominated by covalent and ionic interactions, respectively. Specific systems, namely Si and  $\text{BeF}_2$ , will be considered, as well as the effect of systematically varying a key parameter which controls each respective potential model.

## 2. Models and methods

### (a) Potential models

In the SW potential [14], the energy,  $U$ , is expressed as

$$\left. \begin{aligned} U &= \sum_i \sum_{j>i} U_2(r_{ij}) + \sum_i \sum_{j>i} \sum_{k>j} U_3(r_{ij}, r_{ik}, \theta_{ijk}) \\ U_2(r_{ij}) &= A \left[ B \left( \frac{1}{r_{ij}} \right)^p - \left( \frac{1}{r_{ij}} \right)^q \right] e^{1/(r_{ij}-a)} \\ U_3(r_{ij}, r_{ik}, \theta_{ijk}) &= \lambda [\cos \theta_{ijk} - \cos \theta_0]^2 e^{\gamma/(r_{ij}-a)} e^{\gamma/(r_{ik}-a)}. \end{aligned} \right\} \quad (2.1)$$

and

The atomic interactions are, therefore, controlled by the parameter set  $\{A, \theta_0, B, p, q, a, \lambda, \gamma\}$ . Note that the first term ( $U_2$ ) is a pair potential and would be equivalent to a Lennard–Jones form for  $p = 12$  and  $q = 6$ , modified by an exponential truncation term which effectively removes the high separation dispersive interactions, truncating the pair potential on a length-scale controlled by the parameter  $a$ . The second term ( $U_3$ ) is a three body term which contains the angle between the three bonded atoms labelled  $ijk$ . As a result, the overall potential energy is essentially of the form  $U = U_2 + \lambda U_3$  and so the parameter  $\lambda$  controls the relative magnitude of the two- and three-body terms. Previous work shows that values of  $\lambda = 17$ – $28$  show a density anomaly [46,89]. Furthermore, varying  $\lambda$  has been found to model chemically related systems, notably silicon ( $\lambda = 21$  [14]), phosphorus ( $\lambda \simeq 16.5$  [90,91]), germanium ( $\lambda = 20$  [92]), carbon ( $\lambda = 26.2$  [93]) and even water ( $\lambda = 23.15$  [94]).

For the ionic systems, the potential model used is as described in [8]. Short-range interatomic interactions are accounted for by a modified Born–Mayer [95] potential (see [96] and references therein),

$$U_{sr}(r_{ij}) = B_{ij} e^{-a_{ij}r_{ij}} - \sum_{n=6,8,10\dots} \frac{C_n^{ij}}{r_{ij}^n} f_n(r_{ij}), \quad (2.2)$$

where  $B_{ij}$  and  $a_{ij}$  control the ion radii and the rate of decay of the repulsive wall, respectively,  $C_n^{ij}$  and  $f_n(r_{ij})$  are the dispersion coefficients and respective damping functions [97]) of the form suggested by Tang & Toennies [98]. Full ionic charges ( $\text{Be}^{2+}$ ,  $\text{F}^-$ ) are used throughout.

The pair potential is augmented by a description of ion polarization, introducing a many-body character and modelled using a PIM [80]. In the PIM, the dipole polarizability,  $\alpha$ , and a short-range damping parameter (SRDP) control the magnitude of the induced dipoles [99–101]. The dipole polarizabilities and SRDPs can be obtained from *ab initio* electronic structure calculations [99–103]. Here a model for  $\text{BeF}_2$  is employed which was parameterized by reference to density-functional calculations [8,104]. The full potential parameter set is given in [104]. The anion polarizability,  $\alpha_{\text{F}^-}$ , in  $\text{BeF}_2$  is  $\alpha_{\text{F}^-} = 7.09$  au [8], smaller than the free ion value of  $\alpha_{\text{F}^-}^{\text{FREE}} \sim 16.8$  au [105] as the anion is compressed in the condensed environment [99]. The polarizability of the  $\text{Be}^{2+}$  cation is vanishingly small ( $\alpha_{\text{Be}^{2+}} = 0.052$  au [106]) and sits at the centre of a tetrahedron of anions whose symmetry precludes the formation of electric fields at the cation site. As a result, cation polarization can be neglected.

As noted in the Introduction, the topology of the network (i.e. the order beyond the short-range tetrahedral order) is controlled by the anion polarizability. As a result, it is potentially insightful to consider variations of the  $\text{BeF}_2$  model in which the anion polarizability itself is systematically varied between zero (corresponding to a rigid-ion model—RIM) and the full value of  $\alpha_{\text{F}^-} = 7.09$  au (corresponding to the full PIM). In this work, we employ values of 0, 1, 2, 3, 4, 5, 6 and 7.09 au.

## (b) Methods

To model the covalent systems we employ molecular dynamics (MD) on systems containing 500 atoms, in the NVT ensemble using LAMMPS [107] with the temperature maintained using Nosé–Hoover thermostats [108,109]. Isochores are obtained over a range of volumes and temperatures within the stability limit of the potential model as discussed in [110]. Typically systems are equilibrated for  $t \sim 2$  ns with production runs of  $t \sim 2.5$  ns. We analyse the thermodynamic state space adjacent to the liquid–vapour stability limit using longer production runs of  $t \sim 150$  ns and with increased temperature and volume sampling [2]. At state points for which dynamical arrest was observed on the simulation time-scale replica exchange molecular dynamics (REMD) [111,112] were employed to enable a more complete exploration of the disordered state configurational space and as described in [110]. The thermodynamic data are analysed using the NumPy and SciPy packages [113] and the anomalies and related properties are identified as described in [110]. Note that the liquid–vapour stability limits are identified by isolating the lowest pressure point on an isotherm for each temperature which gives an upper bound estimate of the liquid–vapour spinodal line. As a result this line is referred to as the ‘stability limit’ (SL) rather than the ‘spinodal’.

The location of any liquid–liquid critical points (LLCPs) are estimated from the liquid–liquid spinodals, calculated by identifying pairs of minima and maxima on the isotherms. It should be noted that the presence of such critical points remains controversial. For example, free energy studies indicate that the LLCP locations were previously reported as unstable with respect to a crystalline phase [114]. Our results agree as we are unable to obtain a stable equilibrium in the relevant region of the phase space. The unequilibrated data indicates the existence of two LLCPs in this unstable region, consistent with the concept of ‘virtual criticality’ suggested for water [115]. The existence (or not) of multiple LLCPs does not affect the general discussions presented here.

For the ionic models MD simulations are performed in the NVT ensemble with a system of 576  $\text{MX}_2$  molecules with constant temperature again maintained using Nosé–Hoover thermostats [108,109]. Production runs were on a time-scale of  $t \approx 1$  ns for the RIM and  $t \approx 360$  ps for the PIM, a reflection that a typical PIM simulation requires a computational effort of around an order of magnitude more than the RIM counterpart as a result of evaluating the many-body interactions. The thermodynamic data are extracted and analysed as for the covalent model.

## 3. Summary of anomalous behaviour

A thermodynamic analysis can establish the constraints to describe how the anomaly loci interact. In addition, the analogous analysis indicates how such anomalies interact with related properties such as critical points and stability limits (see, for example, [57] and references therein). The conditions for interaction are obtained directly from the underlying thermodynamic relations using standard manipulations and, as a result, are exact. For clarity, the temperatures of the maxima in the respective properties are referred to as temperature of maximum density (TMD), maximum compressibility (TMC) and maximum heat capacity (TMH), respectively, while the corresponding minima are termed temperature of minimum density, compressibility and heat capacity (TminD, TminC and TminH), respectively.

The key interactions are summarized here:

- Density and compressibility anomaly loci (i.e.  $\text{TMX}$  or  $\text{TminX}$ ,  $X = \{C, D\}$ ) ‘transform’ from a minimum to a maximum when  $(\partial p / \partial T)_{\text{TMX}}$  or  $\text{TminX} = 0$  in the  $pT$  projection. The heat capacity shows the analogous change at  $(\partial p / \partial T)_{\text{TMH}}$  or  $\text{TminH} = \infty$ .
- Although the density anomalies are *not required* to collide with the stability limit, if such a collision occurs then the gradient  $((dp/dT)_{\text{SL}})$  of the stability limit locus at the collision state point is zero, in the  $pT$  projection [57].
- A compressibility anomaly may intersect a density anomaly when the latter has an infinite gradient  $((dp/dT)_{\text{TMD}, \text{TminD}} = \infty)$  in the  $pT$  projection [52].

- Heat capacity anomalies intersect density anomalies when the latter have zero gradient ( $(dp/dT)_{TMD, T_{minD}} = 0$ ) in the  $pT$  projection.
- A heat capacity anomaly locus with zero gradient can only be intersected with an infinite gradient compressibility anomaly.

Regarding the density and compressibility anomalies, the singularity-free interpretation suggests three alternative scenarios for their respective behaviour [52]. The three possibilities differ in the respective relationship of the pressure and temperature at which the TMC and  $T_{minC}$  loci merge compared to the point at which one crosses the density anomaly. A compressibility anomaly locus intercepting the TMD at a positive  $T_{minC}$  gradient is termed TEC1, intersection with a negative gradient is termed TEC3, and a simultaneous TMC/ $T_{minC}$  and intersection with the TMD is termed TEC2.

## 4. Results

The results are divided into those for the specific models for Si and  $BeF_2$ , then extended to more generic models in which the key parameters identified above are systematically varied.

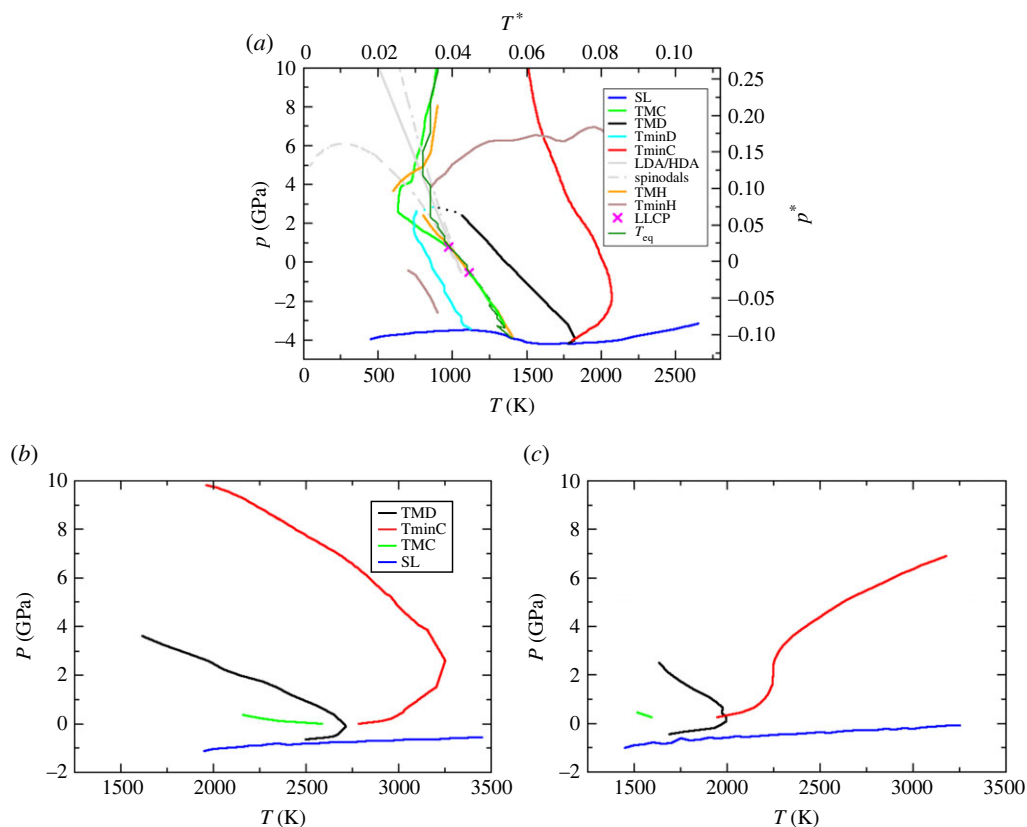
### (a) Specific systems: Si and $BeF_2$

Figure 1*a* shows the locations of a range of thermodynamic anomalies and related properties, obtained using a SW potential parameterized to model silicon.<sup>1</sup> The TMD locus ‘transforms’ to a  $T_{minD}$  at high pressure ( $p \sim 3$  GPa) but does not do so at the low pressure ‘limit’ as both the TMD and  $T_{minD}$  loci intersect the stability limit locus. The high pressure crossover is difficult to observe directly owing to the inherent large fluctuations. The figure shows the extrapolated curves in this region as a guide to the eye. The gradient of the SL locus in the  $pT$  plane is zero at these two intersections, as is required. In the absence of these interactions the TMD/ $T_{minD}$  loci would form a closed loop. The TMD locus is re-entrant with a maximum temperature of  $T \sim 1800$  K. The  $T_{minC}$  and TMC loci intersect the TMD and  $T_{minD}$  loci, respectively, where the density loci have infinite gradient, as required. The compressibility locus intersects the TMD with a positive gradient (equivalent to the TEC1 scenario in the singularity-free interpretation).

Figure 1*a* also highlights the identified pair of virtual LLCs with the TMH locus emerging as required. The heat capacity loci intersect the density anomalies when the latter has zero gradient, again as required and corresponding to the respective TMD $\leftrightarrow$  $T_{minD}$  crossovers. The TMH locus also transforms to the  $T_{minH}$  near the high pressure TMD to  $T_{minD}$  crossover. In addition, at high pressure and temperature the  $T_{minC}$  and  $T_{minH}$  lines intersect with near-orthogonal gradients. Both LLCs and part of the TMH locus that transforms into  $T_{minH}$  are located in the area of the phase diagram where we could not obtain proper equilibrium results. The temperature below which full equilibration is not possible is indicated as  $T_{eq}$  in figure 1.  $T_{eq}$  is determined by observing the arrest in the decay of the time correlation function extracted from the local tetrahedrality (see [110]). The results presented are an attempt to extend the equations of state into unstable parts of the phase diagram in order to obtain a more complete picture of behaviour of thermodynamic anomalies.

Figure 1*a* also shows the LDA/HDA coexistence curve (taken from [86]) along with the two associated spinodals. The coexistence line emerges from an LLC (shown here as originally determined but close to the two current virtual critical points) and appears to go through the density anomaly locus loop at the higher pressure ‘transformation’ between the TMD and  $T_{minD}$ . At higher pressures both the compressibility and heat capacity maxima appear to cross the LDA/HDA coexistence curve. It should be noted, however, that spinodals emanating from an amorphous–amorphous critical point do not interact with the anomalies determined here. The reason for this is that the extracted anomalies ‘live’ on the free energy surface of disordered states

<sup>1</sup>Here, and in subsequent figures, temperatures and pressures are also shown in standard SW reduced units for which  $1T^* = 25\,157$  K and  $1p^* = 36.6$  GPa.



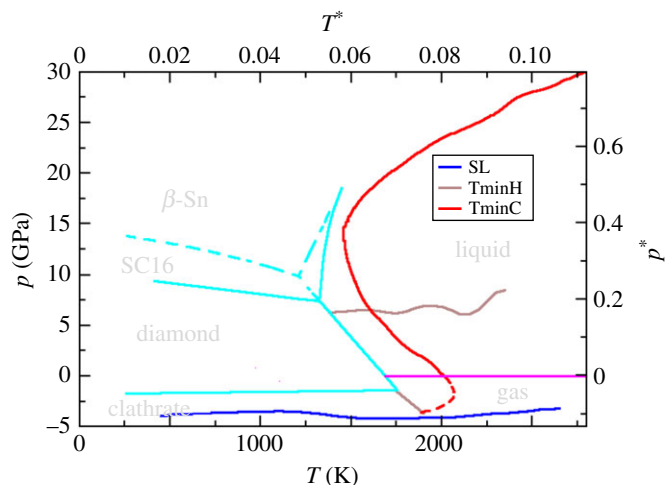
**Figure 1.** The locations of key thermodynamics anomaly loci and related properties for (a) a SW potential appropriate to model Si ( $\lambda = 21$ ), and (b, c) an ionic model for BeF<sub>2</sub> in which the anion polarizability is set to zero ((b), corresponding to a RIM) and in which  $\alpha = 5.0$  au (c). All are shown in the  $pT$  plane. In (a, b), the identities of the specific lines and points are indicated by the legends. In (a), the dashed cyan and black lines show the extrapolation of the TminD and TMD loci at high pressure. The identities of the lines in (c) are equivalent to those in (b). (Online version in colour.)

spanned by all structural (positional) degrees of freedom. The amorphous phases live on a subset of this surface (a subspace) defined by a limited set of configurational variables accessible inside this amorphous phase. This is due to the fact that ergodicity is hindered globally in both cases, for the amorphous phase and for parts of the phase diagram in the supercooled liquid state. However, the amorphous state is just a part of the overall disordered states free energy surface that is again locally hindered from exploring the whole disordered free energy surface.

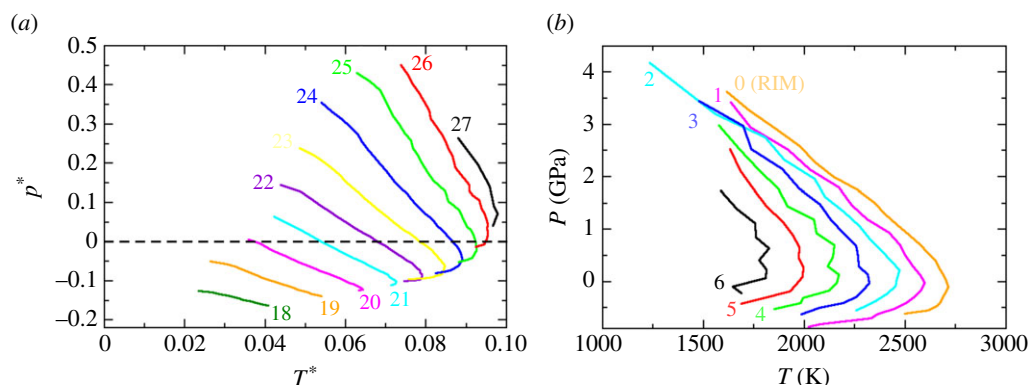
Figure 1 shows a limited range of thermodynamic anomalies obtained for the BeF<sub>2</sub> RIM (i.e.  $\alpha = 0$ —(b)) and the same model with  $\alpha = 5$  au (c). In both cases the TMD locus avoids intersection with the stability limit (and hence the SL gradient does not become zero). Again, the intersection of the respective density and compressibility anomalies occurs at the infinitely sloped part of the TMD. The TMC  $\leftrightarrow$  TminC crossover occurs at a temperature just below the TMD locus for the RIM (corresponding to scenario TEC-I). For the higher polarizability model the crossover shifts to lower temperature. The range of the thermodynamic phase space in which anomalies are observed appears narrower for the electrostatic models than for the covalent models. The effective observation of these anomalies requires the deeply supercooled regime to be traversed. The longer range interactions in the ionic systems mean that suppressing crystallization in these models is more difficult than for the covalent models.

Figure 2 highlights the range over which the anomalies are observed at strict thermodynamic equilibrium (i.e. not in the supercooled regime). The figure also shows the underlying crystalline





**Figure 2.** The thermodynamic anomalies observed for the silicon SW model ( $\lambda = 21$ ) in the fully equilibrated region of the  $pT$  phase space. Anomalies in the compressibility and heat capacity, as well as the stability limit, are shown as indicated by the legend. The figure also highlights the underlying crystal/liquid/gas phase diagram [116]. The liquid/crystal and crystal/crystal phase boundaries are shown in cyan with the dashed lines indicating metastable extensions to include the  $\beta$ -Sn polymorph. The magenta line shows the liquid/gas coexistence curve with the dashed red line highlighting the metastable extension of the TminC locus. (Online version in colour.)



**Figure 3.** The evolution of the TMD loci for the (a) SW model as a function of the parameter  $\lambda$  and (b) the  $\text{BeF}_2$  model as a function of the anion polarizability,  $\alpha$ . In both cases, the respective values of  $\lambda$  and  $\alpha$  (the latter in atomic units) are indicated directly on the figures. The SW model data are shown as a function of the reduced pressure and temperature. (Online version in colour.)

phase diagram (from [116,117]). The phase diagram is shown on an expanded pressure scale compared to figure 1, which highlights the behaviour of the compressibility anomaly locus at high pressure, which shows a characteristic ‘S’ shape, which appears correlated with the liquid/crystal coexistence curves [89]. As a result, the ‘S’ shape arises from the combination of the underlying low pressure diamond crystal/liquid coexistence curve (which shows a negative Clapeyron slope) and the higher pressure SC16 crystal/liquid curve (positive Clapeyron slope).

## (b) General picture

As discussed in §2, a key rationale behind employing relatively simple potential models is the ability to modify the parameters in order to systematically explore the underlying parameter

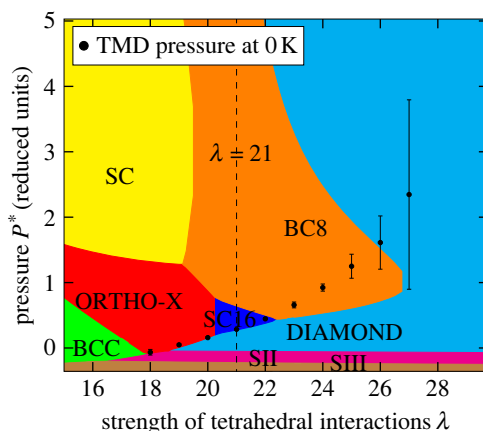


**Figure 4.** Phase diagram (determined at  $T = 0$  K) for the SW potential as a function of the parameter  $\lambda$ . The most stable crystal polymorph is indicated at each  $\{\lambda, p^*\}$  pair. SC refers to a simple cubic phase while SII and SIII are clathrate phases. The black circles represent the pressure limits of the respective TMD loci extracted to zero temperature. (Online version in colour.)

space and hence the fundamental interatomic interactions. In the present work, the structures in our two basic covalent and ionic models are controlled by the parameters  $\lambda$  and  $\alpha$ , respectively. For example, figure 3 shows the change in the respective TMD loci for (a) the SW potential as a function of  $\lambda$ , and (b) the PIM for  $\text{BeF}_2$  as a function of  $\alpha$ . Recall that the parameter  $\lambda$  controls the relative magnitude of the two- and three-body interactions, while the parameter  $\alpha$  controls the spatial relationship between nearest-neighbour tetrahedra. As  $\lambda$  increases the TMD shifts to higher pressure and temperature corresponding to an increase in the strength of the interatomic interactions. For the lowest value of  $\lambda$  for which a TMD can be detected ( $\lambda = 18$ ) the locus appears deep in the supercooled regime and at significant negative pressure and hence only a fragment of the locus appears accessible. Furthermore, the observed TMD is relatively weak in the sense that the respective density maximum has a relatively low curvature. For  $\lambda \sim 20$  the TMD locus becomes re-entrant, a property which is retained up to the highest value for which a TMD is observed ( $\lambda = 27$ ). Figure 3b shows the analogous behaviour for the  $\text{BeF}_2$  model as the anion polarizability,  $\alpha$ , is increased. The TMD remains re-entrant at all values of  $\alpha$  for which it is observed. As  $\alpha$  increases the TMD retracts to lower temperature and becomes weaker and cannot be observed for the full anion polarizability.

To further highlight the relationships between the appearance of the thermodynamic anomalies and the underlying phase diagram, figure 4 shows the  $T = 0$  K phase diagram as a function of pressure and the interaction parameter,  $\lambda$ . The phase diagram is constructed by determining the energy as a function of volume for each possible crystal polymorph, with the pressure obtained from the respective derivatives, and allowing the most favourable free energy to be identified at each state point. The figure also shows the pressures obtained by extending the TMD loci (using a simple linear fit) to  $T = 0$  K. The TMD is only detectable for values of  $\lambda$  for which both low- (tetrahedron-based) and high- (closer-packed) density can be stabilized with pressure. At  $\lambda = 21$ , for example, which corresponds to the Si model discussed above, the diamond and SC16 crystal polymorphs are stable (and which correlate with the characteristic 'S'-shape in the compressibility locus as discussed above).

## 5. Discussion

Figure 5 shows the evolution of the maximum TMD temperature attained as a function of both  $\lambda$  (for the covalent model) and  $\alpha$  (for the ionic model). An increase in  $\lambda$  in the covalent systems appears to have a similar effect to reducing  $\alpha$  in the ionic models as both parameters effectively



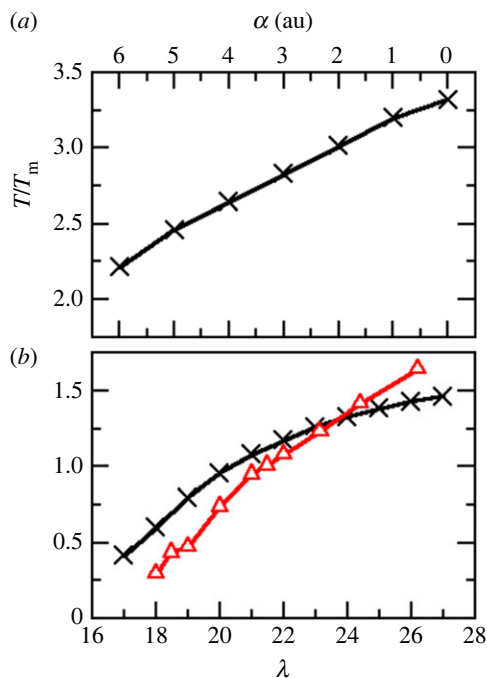


**Figure 5.** The variation of the highest temperature obtained by the TMD locus ( $\times$ , black lines) for the ionic model as function of the anion polarizability,  $\alpha$ , (a), and as a function of the Stillinger–Weber parameter  $\lambda$  for the covalent model (b). In (b), the liquid/crystal coexistence curve from [65] is also shown (red circles). (Online version in colour.)

control the energetic balance between more open and more closed (low and high density) local environments. For the  $\text{BeF}_2$  model employed here the TMD appears well above the likely melting point (i.e.  $T/T_m > 1$ ). However, for the SW potential the TMD lies entirely below the liquid/crystal coexistence curve (which is shown in figure 5 taken from [65]) for  $\lambda \lesssim 24$  and partially emerges from beneath the melting curve for larger values of  $\lambda$ .

Figure 6 shows the TMDs obtained for the  $\text{BeF}_2$  model compared to those obtained for the chemically related systems  $\text{SiO}_2$  and  $\text{GeO}_2$  [61], along with anomalies for  $\text{BeF}_2$  obtained using a different pair potential [61,118]. Analogous data for  $\text{H}_2\text{O}$  is shown for completeness [61]. In each case, the temperature and densities are shown in their respective reduced forms. The temperatures are rescaled using the respective melting points ( $T_m = 813\text{ K}$ ,  $1996\text{ K}$ ,  $1389\text{ K}$  and  $273\text{ K}$  for  $\text{BeF}_2$ ,  $\text{SiO}_2$ ,  $\text{GeO}_2$  and  $\text{H}_2\text{O}$ , respectively—see the references given in [61]) and the number densities are rescaled such that  $\rho^* = n_0\sigma^3$ . The highest temperature reached by the TMD falls from  $\text{BeF}_2 \rightarrow \text{SiO}_2 \rightarrow \text{GeO}_2 \rightarrow \text{H}_2\text{O}$ . The inset to the figure shows the mean M–X–M bond angles,  $\bar{\theta}_{\text{MXM}}$ , that is, the bond angles between neighbouring  $\text{MX}_4$  tetrahedra for the  $\text{BeF}_2$  model over the full range of polarizabilities studied along with experimental values for  $\text{BeF}_2$ ,  $\text{SiO}_2$  and  $\text{GeO}_2$  [77]. There is a clear correlation between the temperature scale at which the TMD locus emerges and the mean inter-tetrahedral bond angle, again as this bond angle is an effective measure of the energetic balance between local high and low density environments.

It is worth emphasizing that the use of relatively simple potential models, in which key interactions are readily identifiable and hence can be manipulated, is central to ‘unpicking’ the factors which control the emergence of the thermodynamic anomalies. In the present work, clear links can be drawn with existing experimental observations (for example, in silicon). It is likely, however, that such anomalies may be observed in more complex systems (for example, in mixtures). A systematic experimental search would be prohibitive but potential model investigations may be more realistic.

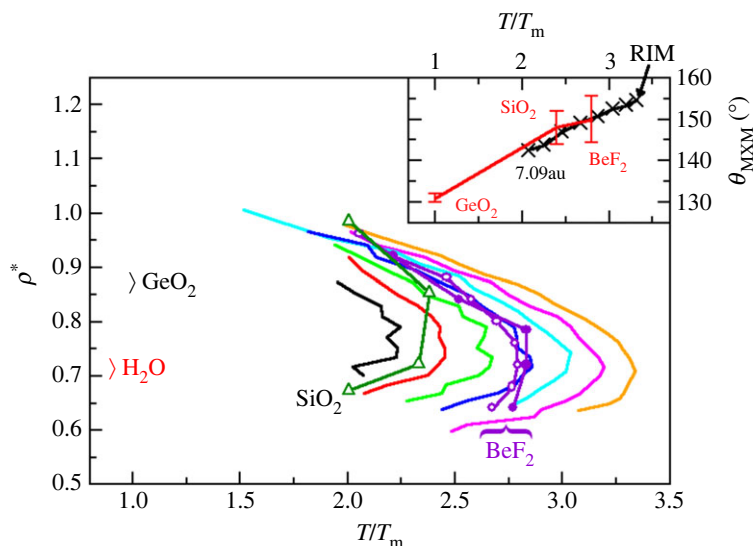


**Figure 6.** Temperature of maximum density loci obtained for the current  $\text{BeF}_2$  model (shown at seven values of the dipole polarizability—colours as for figure 3) and two previous models for  $\text{BeF}_2$  (closed circle from [61] and open circle from [118]), and models for  $\text{SiO}_2$ ,  $\text{GeO}_2$  and  $\text{H}_2\text{O}$  (from [61]) as indicated directly on the figure. In all cases, the abscissa is reduced by the respective melting points and the ordinate is shown as a reduced density. (Online version in colour.)

## 6. Conclusion

In this paper the appearance and evolution in the phase space of thermodynamic anomalies (and related properties) have been studied for two extreme classes of potential models, dominated by covalent and ionic interactions, respectively. In both cases, the potential models have been systematically modified by changing a single key parameter. This simple approach allows the anomalies to be followed to well into the supercooled regime and allows the complex interactions between them to be verified.

**Data accessibility.** This article has no additional data.

**Authors' contributions.** D.F.: conceptualization, data curation, formal analysis, funding acquisition, investigation, methodology, project administration, validation, visualization, writing—original draft, writing—review and editing; M.W.: conceptualization, data curation, formal analysis, funding acquisition, investigation, methodology, project administration, resources, supervision, validation, visualization, writing—original draft, writing—review and editing.

All authors gave final approval for publication and agreed to be held accountable for the work performed therein.

**Conflict of interest declaration.** We declare we have no competing interests.

**Funding.** We are grateful for support from the EPSRC Centre for Doctoral Training in Theory and Modelling in Chemical Sciences (TMCS), under grant no. EP/L015722/1. This paper conforms to the RCUK data management requirements.

**Acknowledgements.** [M.W.] It is a pleasure to acknowledge the enormous influence of Paul McMillan on this work. I first met Paul in Arizona in 1996 and was very fortunate to collaborate with him for over 25 years, including as a colleague at UCL for seven of these years. He was a brilliant scientist with broad interests and huge knowledge. He was also a great friend and I will miss him.

## References

1. Angell CA, Bressel RD, Hemmati M, Sare EJ, Tucker JC. 2000 Water and its anomalies in perspective: tetrahedral liquids with and without liquid–liquid phase transitions. *Phys. Chem. Chem. Phys.* **2**, 1559–1566. (doi:10.1039/b000206m)

2. Vasisht VV, Saw S, Sastry S. 2011 Liquid–liquid critical point in supercooled silicon. *Nat. Phys.* **7**, 549–553. (doi:10.1038/nphys1993)
3. Dhabal D, Chakravarty C, Molinero V, Kashyap HK. 2016 Comparison of liquid-state anomalies in Stillinger-Weber models of water, silicon, and germanium. *J. Chem. Phys.* **145**, 214502. (doi:10.1063/1.4967939)
4. Angell CA, Kanno H. 1973 Density maxima in high-pressure supercooled water and liquid silicon dioxide. *Science* **193**, 1121–1122. (doi:10.1126/science.193.4258.1121)
5. Poole P, Hemmati M, Angell C. 1997 Comparison of thermodynamic properties of simulated liquid silica and water. *Phys. Rev. Lett.* **79**, 2281–2284. (doi:10.1103/PhysRevLett.79.2281)
6. Saika-Voivod I, Sciortino F, Grande T, Poole PH. 2004 Phase diagram of silica from computer simulation. *Phys. Rev. E Stat. Nonlin. Soft Matter. Phys.* **70**, 8. (doi:10.1103/PhysRevE.70.061507)
7. Altabet YE, Singh RS, Stillinger FH, Debenedetti PG. 2017 Thermodynamic anomalies in stretched water. *Langmuir* **33**, 11 771–11 778. (doi:10.1021/acs.langmuir.7b02339)
8. Heaton RJ, Brookes R, Madden PA, Salanne M, Simon C, Turq P. 2006 A first-principles description of liquid BeF<sub>2</sub> and its mixtures with LiF: 1. Potential development and pure BeF<sub>2</sub>. *J. Phys. Chem. B* **110**, 11 454–11 460. (doi:10.1021/jp061000+)
9. Agarwal M, Sharma R, Chakravarty C. 2007 Ionic melts with water like anomalies: thermodynamic properties of liquid BeF<sub>2</sub>. *J. Chem. Phys.* **127**, 164502. (doi:10.1063/1.2794766)
10. Agarwal M, Chakravarty C. 2007 Water like structural and excess entropy anomalies in liquid beryllium fluoride. *J. Phys. Chem. B* **111**, 13 294–13 300. (doi:10.1021/jp0753272)
11. Lascaris E, Hemmati M, Buldyrev SV, Stanley HE, Angell CA. 2014 Search for a liquid-liquid critical point in models of silica. *J. Chem. Phys.* **140**, 1–10. (doi:10.1063/1.4879057)
12. Agarwal M, Alam MP, Chakravarty C. 2011 Thermodynamic, diffusional, and structural anomalies in rigid-body water models. *J. Phys. Chem. B* **115**, 6935–6945. (doi:10.1021/jp110695t)
13. Fijan D, Wilson M. 2020 The progression of thermodynamic anomalies in MX<sub>2</sub> networks with local tetrahedral geometries. *J. Phys.: Condens. Matter* **32**, 275102. (doi:10.1088/1361-648X/ab7d63)
14. Stillinger FH, Weber TA. 1985 Computer simulation of local order in condensed phases of silicon. *Phys. Rev. B* **31**, 5262–5271. (doi:10.1103/PhysRevB.31.5262)
15. Nayar D, Chakravarty C. 2013 Water and water-like liquids: relationships between structure, entropy and mobility. *Phys. Chem. Chem. Phys.* **15**, 14162. (doi:10.1039/c3cp51114f)
16. Stillinger FH, Rahman A. 1974 Improved simulation of liquid water by molecular dynamics. *J. Chem. Phys.* **60**, 1545–1557. (doi:10.1063/1.1681229)
17. Nilsson A, Pettersson LGM. 2015 The structural origin of anomalous properties of liquid water. *Nat. Commun.* **6**, 1–11. (doi:10.1038/ncomms9998)
18. Poole PH, Sciortino F, Essmann U, Stanley HE. 1992 Phase behaviour of metastable water. *Nature* **360**, 324–328. (doi:10.1038/360324a0)
19. Holten V, Limmer DT, Molinero V, Anisimov MA. 2013 Nature of the anomalies in the supercooled liquid state of the mW model of water. *J. Chem. Phys.* **138**, 1–10. (doi:10.1063/1.4802992)
20. Lu J, Qiu Y, Baron R, Molinero V. 2014 Coarse-graining of TIP4P/2005, TIP4P-Ew, SPC/E, and TIP3P to monatomic anisotropic water models using relative entropy minimization. *J. Chem. Theory Comput.* **10**, 4104–4120. (doi:10.1021/ct500487h)
21. Henchman RH, Cockram SJ. 2013 Water's non-tetrahedral side. *Faraday Discuss.* **167**, 529. (doi:10.1039/c3fd00080j)
22. Pallares G, El Mekki Azouzi M, Gonzalez MA, Aragones JL, Abascal JLF, Valeriani C, Caupin F. 2014 Anomalies in bulk supercooled water at negative pressure. *Proc. Natl Acad. Sci. USA* **111**, 7936–7941. (doi:10.1073/pnas.1323366111)
23. Gallo P *et al.* 2016 Water: a tale of two liquids. *Chem. Rev.* **116**, 7463–7500. (doi:10.1021/acs.chemrev.5b00750)
24. Pallares G, Gonzalez MA, Abascal JLF, Valeriani C, Caupin F. 2016 Equation of state for water and its line of density maxima down to 120 MPa. *Phys. Chem. Chem. Phys.* **18**, 5896–5900. (doi:10.1039/C5CP07580G)
25. Liu Y, Palmer JC, Panagiotopoulos AZ, Debenedetti PG. 2012 Liquid-liquid transition in ST2 water. *J. Chem. Phys.* **137**, 214505. (doi:10.1063/1.4769126)

26. Russo J, Tanaka H. 2014 Understanding water's anomalies with locally favoured structures. *Nat. Commun.* **5**, 3556. (doi:10.1038/ncomms4556)
27. González MA, Valeriani C, Caupin F, Abascal JLF. 2016 A comprehensive scenario of the thermodynamic anomalies of water using the TIP4P/2005 model. *J. Chem. Phys.* **145**, 054505. (doi:10.1063/1.4960185)
28. Palmer JC, Poole PH, Sciortino F, Debenedetti PG. 2018 Advances in computational studies of the liquid-liquid transition in water and water-like models. *Chem. Rev.* **118**, 9129–9151. (doi:10.1021/acs.chemrev.8b00228)
29. Poole PH, Bowles RK, Saika-Voivod I, Sciortino F. 2013 Free energy surface of ST2 water near the liquid-liquid phase transition. *J. Chem. Phys.* **138**, 034505. (doi:10.1063/1.4775738)
30. Tombari E, Ferrari C, Salvetti G. 1999 Heat capacity anomaly in a large sample of supercooled water. *Chem. Phys. Lett.* **300**, 749–751. (doi:10.1016/S0009-2614(98)01392-X)
31. Caupin F. 2015 Escaping the no man's land: recent experiments on metastable liquid water. *J. Non-Cryst. Solids* **407**, 441–448. (doi:10.1016/j.jnoncrysol.2014.09.037)
32. Yan Z, Buldyrev SV, Stanley HE. 2008 Relation of water anomalies to the excess entropy. *Phys. Rev. E* **78**, 1–5. (doi:10.1103/PhysRevE.78.051201)
33. Shadrack Jabes B, Nayar D, Dhabal D, Molinero V, Chakravarty C. 2012 Water and other tetrahedral liquids: order, anomalies and solvation. *J. Phys. Condens. Matter* **24**, 284116. (doi:10.1088/0953-8984/24/28/284116)
34. Caupin F, Anisimov MA. 2019 Thermodynamics of supercooled and stretched water: unifying two-structure description and liquid-vapor spinodal. *J. Chem. Phys.* **151**, 34503. (doi:10.1063/1.5100228)
35. Wu Y, Tepper HL, Voth GA. 2006 Flexible simple point-charge water model with improved liquid-state properties. *J. Chem. Phys.* **124**, 024503. (doi:10.1063/1.2136877)
36. Poole PH, Sciortino F, Essmann U, Stanley HE. 1993 Spinodal of liquid water. *Phys. Rev. E* **48**, 3799–3817. (doi:10.1103/PhysRevE.48.3799)
37. Speedy RJ. 1982 Stability-limit conjecture. An interpretation of the properties of water. *J. Phys. Chem.* **86**, 982–991. (doi:10.1007/s00542-005-0004-z)
38. Palmer JC, Martelli F, Liu Y, Car R, Panagiotopoulos AZ, Debenedetti PG. 2014 Metastable liquid–liquid transition in a molecular model of water. *Nature* **510**, 385–388. (doi:10.1038/nature13405)
39. Angell CA, Shuppert J, Tucker JC. 1973 Anomalous properties of supercooled water. Heat capacity, expansivity, and proton magnetic resonance chemical shift from 0 to –38%. *J. Phys. Chem.* **77**, 3092–3099. (doi:10.1021/j100644a014)
40. Wang Z, Ito K, Leão JB, Harriger L, Liu Y, Chen SH. 2015 Liquid–liquid phase transition and its phase diagram in deeply-cooled heavy water confined in a nanoporous silica matrix. *J. Phys. Chem. Lett.* **6**, 2009–2014. (doi:10.1021/acs.jpcllett.5b00827)
41. Sciortino F, Saika-Voivod I, Poole PH. 2011 Study of the ST2 model of water close to the liquid–liquid critical point. *Phys. Chem. Chem. Phys.* **13**, 19759. (doi:10.1039/c1cp22316j)
42. Holten V, Palmer JC, Poole PH, Debenedetti PG, Anisimov MA. 2014 Two-state thermodynamics of the ST2 model for supercooled water. *J. Chem. Phys.* **140**, 104502. (doi:10.1063/1.4867287)
43. Shiratani E, Sasai M. 1996 Growth and collapse of structural patterns in the hydrogen bond network in liquid water. *J. Chem. Phys.* **104**, 7671–7680. (doi:10.1063/1.471475)
44. Tanaka H. 2000 Thermodynamic anomaly and polyamorphism of water. *Europhys. Lett.* **50**, 340–346. (doi:10.1209/epl/i2000-00276-4)
45. Skinner LB, Benmore CJ, Neuefeind JC, Parise JB. 2014 The structure of water around the compressibility minimum. *J. Chem. Phys.* **141**, 214507. (doi:10.1063/1.4902412)
46. Singh RS, Biddle JW, Debenedetti PG, Anisimov MA. 2016 Two-state thermodynamics and the possibility of a liquid-liquid phase transition in supercooled TIP4P/2005 water Two-state thermodynamics and the possibility of a liquid-liquid phase transition in supercooled TIP4P/2005 water. *J. Chem. Phys.* **144**, 144504. (doi:10.1063/1.4944986)
47. Holten V, Kalov J, Anisimov MA, Sengers JV. 2012 Thermodynamics of liquid-liquid criticality in supercooled water in a mean-field approximation. *Int. J. Thermophys.* **33**, 758–773. (doi:10.1007/s10765-012-1195-z)
48. Bertrand CE, Anisimov MA. 2011 Peculiar thermodynamics of the second critical point in supercooled water. *J. Phys. Chem. B* **115**, 14 099–14 111. (doi:10.1021/jp204011z)

49. Poole PH, Saika-Voivod I, Sciortino F. 2005 Density minimum and liquid–liquid phase transition. *J. Phys.: Condens. Matter* **17**, L431–L437. (doi:10.1088/0953-8984/17/43/L01)
50. Holten V, Qiu C, Guillerme E, Wilke M, Rička J, Frenz M, Caupin F. 2017 Compressibility anomalies in stretched water and their interplay with density anomalies. *J. Phys. Chem. Lett.* **8**, 5519–5522. (doi:10.1021/acs.jpclett.7b02563)
51. Debenedetti PG, D’Antonio MC. 1988 Stability and tensile strength of liquids exhibiting density maxima. *AIChE J.* **34**, 447–455. (doi:10.1002/aic.690340312)
52. Sastry S, Debenedetti PG, Sciortino F, Stanley HE. 1996 Singularity-free interpretation of the thermodynamics of supercooled water. *Phys. Rev. E* **53**, 6144–6154. (doi:10.1063/1.476600)
53. Debenedetti PG, D’Antonio MC. 1986a On the nature of the tensile instability in metastable liquids and its relationship to density anomalies. *J. Chem. Phys.* **84**, 3339–3345. (doi:10.1063/1.450269)
54. Debenedetti PG, D’Antonio MC. 1986b On the entropy changes and fluctuations occurring near a tensile instability. *J. Chem. Phys.* **85**, 4005–4010. (doi:10.1063/1.450923)
55. Chitnelawong P, Sciortino F, Poole PH. 2019 The stability-limit conjecture revisited. *J. Chem. Phys.* **150**, 234503. (doi:10.1063/1.5100129)
56. Rovigatti L, Bianco V, Tavares JM, Sciortino F. 2017 Communication: re-entrant limits of stability of the liquid phase and the Speedy scenario in colloidal model systems. *J. Chem. Phys.* **146**, 041103. (doi:10.1063/1.4974830)
57. Fijan D, Wilson M. 2019 The interactions between thermodynamic anomalies. *J. Chem. Phys.* **151**, 24502. (doi:10.1063/1.5103242)
58. Shell MS, Debenedetti PG, Panagiotopoulos AZ. 2002 Molecular structural order and anomalies in liquid silica. *Phys. Rev. E* **66**, 1–8. (doi:10.1103/PhysRevE.66.011202)
59. Saika-Voivod I, Sciortino F, Poole PH. 2000 Computer simulations of liquid silica: equation of state and liquid–liquid phase transition. *Phys. Rev. E* **63**, 011202. (doi:10.1103/PhysRevE.63.011202)
60. Sharma BK, Wilson M. 2006 Intermediate-range order in molten network-forming systems. *Phys. Rev. B* **73**, 1–4. (doi:10.1103/PhysRevB.73.060201)
61. Jabes BS, Agarwal M, Chakravarty C. 2010 Tetrahedral order, pair correlation entropy, and water like liquid state anomalies: comparison of GeO<sub>2</sub> with BeF<sub>2</sub>, SiO<sub>2</sub>, and H<sub>2</sub>O. *J. Chem. Phys.* **132**, 234507. (doi:10.1063/1.3439593)
62. Debenedetti PG. 2003 Supercooled and glassy water. *J. Phys. Condens. Matter* **15**, 1669–1726. (doi:10.1088/0953-8984/15/45/R01)
63. Errington JR, Debenedetti PG. 2001 Relationship between structural order and the anomalies of liquid water. *Nature* **409**, 318–321. (doi:10.1038/35053024)
64. Cisneros GA *et al.* 2016 Modeling molecular interactions in water: from pairwise to many-body potential energy functions. *Chem. Rev.* **116**, 7501–7528. (doi:10.1021/acs.chemrev.5b00644)
65. Molinero V, Sastry S, Angell CA. 2006 Tuning of tetrahedrality in a silicon potential yields a series of monatomic (Metal-like) glass formers of very high fragility. *Phys. Rev. Lett.* **97**, 1–4. (doi:10.1103/PhysRevLett.97.075701)
66. Hujo W, Jabes BS, Rana VK, Chakravarty C, Molinero V. 2011 The rise and fall of anomalies in tetrahedral liquids. *J. Stat. Phys.* **145**, 293–312. (doi:10.1007/s10955-011-0293-9)
67. Sadr-Lahijany MR, Scala A, Buldyrev SV, Stanley HE. 1998 Liquid-state anomalies and the Stell-Hemmer core-softened potential. *Phys. Rev. Lett.* **81**, 4895–4898. (doi:10.1103/PhysRevLett.81.4895)
68. Wilding NB, Magee JE. 2002 Phase behavior and thermodynamic anomalies of core-softened fluids. *Phys. Rev. E* **66**, 031509. (doi:10.1103/PhysRevE.66.031509)
69. Gibson HM, Wilding NB. 2006 Metastable liquid–liquid coexistence and density anomalies in a core-softened fluid. *Phys. Rev. E* **73**, 061507. (doi:10.1103/PhysRevE.73.061507)
70. Salcedo E, de Oliveira AB, Barraz NM, Chakravarty C, Barbosa MC. 2011 Core-softened fluids, water-like anomalies, and the liquid–liquid critical points. *J. Chem. Phys.* **135**, 044517. (doi:10.1063/1.3613669)
71. Smallenburg F, Filion L, Sciortino F. 2015 Liquid–liquid phase transitions in tetrahedrally coordinated fluids via wertheim theory. *J. Phys. Chem. B* **119**, 9076–9083. (doi:10.1021/jp508788m)



72. Smallenburg F, Sciortino F. 2015 Tuning the liquid-liquid transition by modulating the hydrogen-bond angular flexibility in a model for water. *Phys. Rev. Lett.* **115**, 015701. (doi:10.1103/PhysRevLett.115.015701)
73. March N, Tosi MP. 1984 *Coulomb liquids*. Cambridge, UK: Academic Press.
74. Hansen JP, McDonald I. 1986 *Theory of simple liquids*. New York, NY: Academic Press.
75. Rovere M, Tosi MP. 1986 Structure and dynamics of molten salts. *Rep. Prog. Phys.* **49**, 1001–1081. (doi:10.1088/0034-4885/49/9/002)
76. Ubbelohde AR. 1978 *The molten state of matter*. Oxford, UK: John Wiley and Sons.
77. Desa J. 1982 A neutron diffraction investigation of the structure of vitreous zinc chloride. *J. Non-Cryst. Solids* **51**, 57–86. (doi:10.1016/0022-3093(82)90189-2)
78. Wilson M. 2015 *Molecular dynamics simulations of disordered materials*. New York, NY: Springer.
79. Salmon PS, Zeidler A. 2019 Ordering on different length scales in liquid and amorphous materials. *J. Stat. Mech.* **2019**, 114006. (doi:10.1088/1742-5468/ab3cce)
80. Madden PA, Wilson M. 1996 ‘Covalent’ effects in ‘Ionic’ systems. *Chem. Soc. Rev.* **25**, 339–350. (doi:10.1039/CS9962500339)
81. Wilson M, Salmon PS. 2009 Network topology and the fragility of tetrahedral glass-forming liquids. *Phys. Rev. Lett.* **103**, 1–4. (doi:10.1103/PhysRevLett.103.157801)
82. Wilson M, Sharma BK. 2008 The evolution of intermediate-range order in molten network-forming materials. *J. Chem. Phys.* **128**, 214507. (doi:10.1063/1.2931936)
83. Marrocchelli D, Salanne M, Madden PA, Simon C, Turq P. 2009 The construction of a reliable potential for GeO<sub>2</sub> from first principles. *Mol. Phys.* **107**, 443–452. (doi:10.1080/00268970902845347)
84. Sharma BK, Wilson M. 2008 Polyamorphism and the evolution of intermediate-range order in molten ZnCl<sub>2</sub>. *J. Phys.: Condens. Matter* **20**, 244123. (doi:10.1088/0953-8984/20/24/244123)
85. Corradini D, Ishii Y, Ohtori N, Salanne M. 2015 DFT-based polarizable force field for TiO<sub>2</sub> and SiO<sub>2</sub>. *Model. Simul. Mater. Sci. Eng.* **23**, 074005. (doi:10.1088/0965-0393/23/7/074005)
86. McMillan PF, Wilson M, Daisenberger D, Machon D. 2005 A density-driven phase transition between semiconducting and metallic polyamorphs of silicon. *Nat. Mater.* **4**, 680–684. (doi:10.1038/nmat1458)
87. Deringer V, Bernstein N, Csányi G, Wilson M, Drabold D, Elliott S. 2021 Origins of structural and electronic transitions in disordered silicon. *Nature* **589**, 59–64. (doi:10.1038/s41586-020-03072-z)
88. Durandurdu M, Drabold DA. 2001 Ab initio simulation of first-order amorphous-to-amorphous phase transition of silicon. *Phys. Rev. B* **64**, 014101. (doi:10.1103/PhysRevB.64.014101)
89. Fijan D, Wilson M. 2019 Liquid state anomalies and the relationship to the crystalline phase diagram. *Phys. Rev. E* **99**, 010103. (doi:10.1103/PhysRevE.99.010103)
90. Jiang JW, Rabczuk T, Park HS. 2015 A Stillinger-Weber potential for single-layered black phosphorus, and the importance of cross-pucker interactions for a negative Poisson’s ratio and edge stress-induced bending. *Nanoscale* **7**, 6059–6068. (doi:10.1039/C4NR07341J)
91. Jiang JW. 2015 Parametrization of Stillinger-Weber potential based on valence force field model: application to single-layer MoS<sub>2</sub> and black phosphorus. *Nanotechnology* **26**, 315706. (doi:10.1088/0957-4484/26/31/315706)
92. Bhat MH, Molinero V, Soignard E, Solomon VC, Sastry S, Yarger JL, Angell CA. 2007 Vitrification of a monatomic metallic liquid. *Nature* **448**, 787–790. (doi:10.1038/nature06044)
93. Barnard AS, Russo SP. 2002 Development of an improved Stillinger-Weber potential for tetrahedral carbon using ab initio (Hartree-Fock and MP2) methods. *Mol. Phys.* **100**, 1517–1525. (doi:10.1080/00268970110109853)
94. Molinero V, Moore EB. 2009 Water modeled as an intermediate element between carbon and silicon. *J. Phys. Chem. B* **113**, 4008–4016. (doi:10.1021/jp805227c)
95. Born M, Mayer JE. 1932 Zur Gittertheorie der Ionenkristalle. *Z. Phys.* **75**, 1–18. (doi:10.1007/BF01340511)
96. Sangster MJL, Dixon M. 1976 Interionic potentials in alkali Halides and their use in simulations of the molten salts. *Adv. Phys.* **25**, 247–342. (doi:10.1080/00018737600101392)
97. Stone AJ. 1996 *Theory of intermolecular forces*. Oxford, UK: Oxford University Press.



98. Tang K, Toennies J. 1984 An improved simple model for the van der Waals potential based on universal damping functions for the dispersion coefficients. *J. Chem. Phys.* **80**, 3726–3741. (doi:10.1063/1.447150)
99. Jemmer P, Fowler PW, Wilson M, Madden PA. 1999 Dipole and quadrupole polarization in ionic systems: ab initio studies. *J. Chem. Phys.* **111**, 2038–2049. (doi:10.1063/1.479472)
100. Domene C, Fowler PW, Madden PA, Wilson M, Wheatley RJ. 2001 Overlap-model and ab initio cluster calculations of ion properties in distorted environments. *Chem. Phys. Lett.* **333**, 403–412. (doi:10.1016/S0009-2614(00)01389-0)
101. Domene C, Fowler PW, Madden PA, Xu J, Wheatley RJ, Wilson M. 2001 Short-range contributions to the polarization of cations. *J. Phys. Chem. A* **105**, 4136–4142. (doi:10.1021/jp004173m)
102. Fowler PW, Madden PA. 1985 Fluctuating dipoles and polarizabilities in ionic materials: calculations on LiF. *Phys. Rev. B* **31**, 5443–5455. (doi:10.1103/PhysRevB.31.5443)
103. Aguado A, Bernasconi L, Jahn S, Madden PA. 2003 Multipoles and interaction potentials in ionic materials from planewave-DFT calculations. *Faraday Discuss.* **124**, 171. (doi:10.1039/B300319C)
104. Salanne M, Simon C, Turq P, Heaton RJ, Madden PA. 2006 A first-principles description of liquid BeF<sub>2</sub> and its mixtures with LiF: 2. Network formation in LiF-BeF<sub>2</sub>. *J. Phys. Chem. B* **110**, 11 461–11 467. (doi:10.1021/jp061002u)
105. Jemmer P, Fowler PW, Wilson M, Madden PA. 1998 Environmental effects on anion polarizability: variation with lattice parameter and coordination number. *J. Phys. Chem. A* **102**, 8377–8385. (doi:10.1021/jp982029j)
106. Pyper NC. 1991 Ab-initio calculations of inter-ionic potentials and the cohesive properties of ionic solids. *Adv. Solid State Chem.* **2**, 223.
107. Plimpton S. 1995 Fast parallel algorithms for short—range molecular dynamics. *J. Comput. Phys.* **117**, 1–19. (doi:10.1006/jcph.1995.1039)
108. Nosé S. 1984 A unified formulation of the constant temperature molecular dynamics methods. *J. Chem. Phys.* **81**, 511–519. (doi:10.1063/1.447334)
109. Hoover WG. 1985 Canonical dynamics: equilibrium phase-space distributions. *Phys. Rev. A* **31**, 1695–1697. (doi:10.1103/PhysRevA.31.1695)
110. Fijan D, Wilson M. 2021 Thermodynamic anomalies in silicon and the relationship to the phase diagram. *J. Phys.: Condens. Matter* **33**, 425404. (doi:10.1088/1361-648X/ac16f5)
111. Sugita Y, Okamoto Y. 1999 Replica-exchange molecular dynamics method for protein folding. *Chem. Phys. Lett.* **314**, 141–151. (doi:10.1016/S0009-2614(99)01123-9)
112. Swendsen R, Wang J. 1986 Replica Monte Carlo simulation of spin glasses. *Phys. Rev. Lett.* **57**, 2607–2609. (doi:10.1103/PhysRevLett.57.2607)
113. Jones E, Oliphant T, Peterson P. 2001 SciPy: open source scientific tools for python.
114. Ricci F, Palmer JC, Goswami Y, Sastry S, Angell CA, Debenedetti PG. 2019 A computational investigation of the thermodynamics of the Stillinger-Weber family of models at supercooled conditions. *Mol. Phys.* **117**, 3254–3268. (doi:DOI:10.1080/00268976.2019.1649496)
115. Holten V, Bertrand C, Anisimov MA, Sengers JV. 2012 Thermodynamics of supercooled water. *J. Chem. Phys.* **136**, 094507. (doi:10.1063/1.3690497)
116. Romano F, Russo J, Tanaka H. 2014 Novel stable crystalline phase for the Stillinger-Weber potential. *Phys. Rev. B: Condens. Matter* **90**, 014204. (doi:10.1103/PhysRevB.90.014204)
117. Daisenberger D, McMillan PF, Wilson M. 2010 Crystal-liquid interfaces and phase relations in stable and metastable silicon at positive and negative pressure. *Phys. Rev. B* **82**, 214101. (doi:10.1103/PhysRevB.82.214101)
118. Hemmati M, Moynihan CT, Angell CA. 2001 Interpretation of the molten BeF<sub>2</sub> viscosity anomaly in terms of a high temperature density maximum, and other waterlike features. *J. Chem. Phys.* **115**, 6663–6671. (doi:10.1063/1.1396679)